REPORT DOCUMENTATION PAGE

1a. REPORT SECURITY CLASSIFICATION Unclassified	1b. RESTRICTIVE MARKINGS
2a. SECURITY CLASSIFICATION AUTHORITY	3. DISTRIBUTION/AVAILABILITY OF REPORT Approved for public release; distribution is unlimited.
2b. DECLASSIFICATION/DOWNGRADING SCHEDULE	
4. PERFORMING ORGANIZATION REPORT NUMBER(S)	5. MONITORING ORGANIZATION REPORT NUMBER(S)
6a. NAME OF PERFORMING ORGANIZATION Naval Postgraduate School 6b. OFFICE SYMBOL *(If applicable)* 31	7a. NAME OF MONITORING ORGANIZATION Naval Postgraduate School
6c. ADDRESS *(City, State, and ZIP Code)* Monterey, CA 93943-5000	7b. ADDRESS *(City, State, and ZIP Code)* Monterey, CA 93943-5000
8a. NAME OF FUNDING/SPONSORING ORGANIZATION 8b. OFFICE SYMBOL *(If applicable)*	9. PROCUREMENT INSTRUMENT IDENTIFICATION NUMBER
8c. ADDRESS *(City, State, and ZIP Code)*	10. SOURCE OF FUNDING NUMBERS Program Element No. / Project No. / Task No. / Work Unit Accession Number

11. TITLE *(Include Security Classification)*
Implementation and Use of a Computational Ray-Tracing Program for the Design and Analysis of Complex Optical Systems

12. PERSONAL AUTHOR(S) Atkinson, J. Dudley IV

13a. TYPE OF REPORT	13b. TIME COVERED	14. DATE OF REPORT *(year, month, day)*	15. PAGE COUNT
Master's Thesis	From To	March 1993	55

16. SUPPLEMENTARY NOTATION
The views expressed in this thesis are those of the author and do not reflect the official policy or position of the Department of Defense or the U.S. Government.

17. COSATI CODES			18. SUBJECT TERMS *(continue on reverse if necessary and identify by block number)*
FIELD	GROUP	SUBGROUP	Ray Tracing; Spectrograph; Interferometer

19. ABSTRACT *(continue on reverse if necessary and identify by block number)*

A new ray-tracing computer program is presented as an analysis and design tool for the development of complex optical systems. The algorithms for the ray-tracing are presented for a wide variety of optical systems surface types. Unique methods for the prediction of two-beam interference patterns are implemented so that amplitude-splitting interferometers can be modeled. Modules for line shape analysis and data storage are also described. This program (DART) is validated using the previously established characteristics of the Middle Ultraviolet Spectral Analysis of Nitrogen Gasses (MUSTANG) instrument, which has a resolution of 10 Å, an X-axis field-of-view of 1.2 milliradians, a Y-axis field-of-view of 37 milliradians, and a 1600 Å bandpass. DART is used to predict the optical characteristics of a new instrument, ISAAC, that is planned for satellite deployment in 1995. The full wavelength range of ISAAC is 1250 Å, and the instantaneous band-pass is approximately 250 Å. The full wavelength coverage is obtained by rotating a reflection grating in five discreet steps. Based on the DART calculations, the resolution of the ISAAC instrument will exceed 1.30 Å for all bands, with resolutions as low as 1.06 Å at the longer wavelengths. The predicted X-axis field-of-view is 0.5 milliradians and the Y-axis field-of-view is 36 milliradians.

20. DISTRIBUTION/AVAILABILITY OF ABSTRACT	21. ABSTRACT SECURITY CLASSIFICATION	
☒ UNCLASSIFIED/UNLIMITED ☐ SAME AS REPORT ☐ DTIC USERS	Unclassified	
22a. NAME OF RESPONSIBLE INDIVIDUAL David D. Cleary	22b. TELEPHONE *(Include Area code)* (408) 656-2828	22c. OFFICE SYMBOL PH/Cl

DD FORM 1473, Jun 86 83 APR edition may be used until exhausted
All other editions are obsolete

T260189

Approved for public release; distribution is unlimited.

Implementation and Use of a Computational Ray-Tracing Program for the Design and Analysis of Complex Optical Systems

by

J. Dudley Atkinson IV
Lieutenant, United States Navy
B.S., Louisiana State University

Submitted in partial fulfillment of the requirements for the degrees of

MASTER OF SCIENCE IN PHYSICS
and
MASTER OF SCIENCE IN ENGINEERING SCIENCE (ASTRONAUTICS)

from the
NAVAL POSTGRADUATE SCHOOL
March, 1993

ABSTRACT

A new ray-tracing computer program is presented as an analysis and design tool for the development of complex optical systems. The algorithms for the ray-tracing are presented for a wide variety of optical surface types. Unique methods for the prediction of two-beam interference patterns are implemented so that amplitude-splitting interferometers can be modeled. Modules for line shape analysis and data storage are also described. This program (DART) is validated using the previously established characteristics of the Middle Ultraviolet Spectral Analysis of Nitrogen Gasses (MUSTANG) instrument, which has a resolution of 10 Å, an X-axis field-of-view of 1.2 milliradians, a Y-axis field-of-view of 37 milliradians, and a 1600 Å band-pass. DART is used to predict the optical characteristics of a new instrument, ISAAC, that is planned for satellite deployment in 1995. The full wavelength range of ISAAC is 1250 Å, and the instantaneous band-pass is approximately 250 Å. The full wavelength coverage is obtained by rotating a reflection grating in five discreet steps. Based on the DART calculations, the resolution of the ISAAC instrument will exceed 1.30 Å for all bands, with resolutions as low a 1.06 Å at the longer wavelengths. The predicted X-axis field-of-view is 0.5 milliradians and the Y-axis field-of-view is 36 milliradians.

C.1

TABLE OF CONTENTS

I. INTRODUCTION 1
II. RAY TRACING FUNDAMENTALS 4
A. COORDINATE SYSTEMS AND RAY TRACE INITIALIZATION 4
1. Coordinate Systems 4
a. Global Coordinates 4
b. Local Coordinates 5
2. Direction Cosines 5
3. Aperture Ray Generation 6
4. General Outline of the Tracing Procedure 6
B. ELEMENT ANALYSIS 7
1. The Most General Intercept Solution 7
2. Intercepts for Special Cases 8
a. Planar Elements 9
b. Spherical Elements 9
c. Cylindrical Elements 10
d. Eliptical Elements 10
e. Parabolic Elements 11
3. Factors Needed To Find Direction Changes After Intersection 11
4. The Most General Direction Cosine Solutions 12
a. Refraction 12
b. Reflection 13
c. Grating Characteristics 13
d. Refraction Solutions for Gratings 14
5. Direction Cosines in DART. 15
III. DART MODULES 16
A. LAYOUT MODULE 16
B. DATA STORAGE MODULES 16
C. FULL WIDTH AT HALF MAXIMUM 18
D. INTERFERENCE MODULE 19
1. Key Ideas For Interference Computation. 20
2. The Interference Algorithm 22
3. Limitations of the Interference Routine. 23
IV. ANALYSIS OF THE MUSTANG 25
A. DESCRIPTION OF MUSTANG 25
B. ANALYTICAL RESULTS 27
1. Line Placement 27
2. Detector Resolution 29
3. Field-of-View 30
V. MUSTANG ON ORBIT (ISAAC) 33
A. DESIGN CHANGES 33

1. The New Grating 33
2. The Narrower Slit 36
3. The Parabolic Telescope Mirror 36
4. The Grating Adjustment 37
B. DETAILED ANALYSIS 38
1. Line Placement 39
2. Resolution Measurements 39
3. Field-of-View 40
VI. CONCLUSIONS AND RECOMMENDATIONS 45
LIST OF REFERENCES 47
INITIAL DISTRIBUTION LIST 48

I. INTRODUCTION

The study of optical systems has been of great interest for several centuries, first for telescopes and later for everything from microscopes to lighthouses. Before the advent of fast computers, optical systems were designed using mathematical formulae that described the optical wavefront and the changes induced by the various elements in the light path. This method can be very rigorous or it can make broad assumptions to determine macrosopic properties of a system, but in the main it is a very tedious and time-consuming task to wade through the required symbol manipulation. Because of this difficulty, many insightful schemes have been devised to linearize and simplify the physical characteristics of optical systems so that they can be readily understood and used without lengthy computation. An alternate method of analyzing these systems is to study the light ray by ray, by splitting the light entering the system into a finite number of beams, tracing each of these rays from element to element, and finally reassembling the rays into a single object that represents the output of the system.

The disadvantage of this approach is that for complex systems, the time involved in completing the analysis is still very considerable. But since fast computational devices are readily available, and since computers favor numerical processing over symbol manipulation, the ray approach is a natural choice for optical system design and analysis. This thesis presents one computational method ideally suited to this task. Spencer and Murty (1962) outlined the mathematical basis for tracing skew rays through systems of arbitrary complexity, with four primary goals:

(1) Cylindrical, toric, and conic surfaces must be accommodated with provision for specifying departures from these forms.

(2) Provision must be made for the arbitrary orientation and positioning of all surfaces with relative ease of specification.

(3) Diffraction gratings generated by linear or concentric circular ruling motions on any of the allowed surface types must be accommodated with provision for specifying a variable ruling separation.

(4) The procedure should be capable of extension to cover new surface types or new modes of ruling without major modification.

This thesis uses the methods of Spencer and Murty as the foundation for applied computational algorithms, which will be summarized below. This thesis also adds extensively to the earlier work done by the Naval Research Laboratory (D. Prinz, private communication, 1991), which implemented the methods of Spencer and Murty in a mainframe computing package written in the FORTRAN language and who clearly spelled out the steps required in the creation of complex surface solutions.

This work is centered upon creating an interactive tool that combined the physics and modeling required for complex raytracing with quick processing and useful visual display, capable of not only tracing solutions but analysis of the generated images as well. This program is written in the Turbo Pascal language for operation under the Windows shell on a common IBM compatible desktop computer, and is named DART (Dudley Atkinson Ray Tracer). It is a complete implementation of the Spencer and Murty formulas, and produces a visual screen display of the image the modeled optical system should produce. It is very flexible in the number and type of system inputs allowed, and can produce output data in a variety of formats for use in other packages. A layout of the modelled system can be drawn by the computer, and the rays that are traced through the system can be drawn on the layout for detailed analysis. Modules are included to compute resolution data in the form of full width at half maximum (FWHM), and interference patterns resulting from two-beam systems can also be generated for display. This implementation is very flexible and can easily be extended to add any number of analysis tools with only a small amount of additional programming. After detailing the basic procedures for system and element raytracing, and after outlining the specific implementation of these routines, this thesis validates the models using a known optical instrument: the NPS MUSTANG. This instrument was developed to study low-intensity ultraviolet emissions from the atmosphere in an attempt to characterize the ionospheric properties that are important in electromagnetic wave propagation. The MUSTANG

instrument is described in detail in Chaper IV. Because the optical characteristics of the MUSTANG are well known (Anderson, 1990; Chase, 1992) and because the instrument uses a variety of complex optical elements, this instrument provides a unique resource for DART validation.

The MUSTANG is scheduled for satellite deployment in 1995. The instrument will be changed significantly for this long-duration mission in order to improve the resolution of the device. The design changes needed for this mission have been modeled and analyzed using DART in order to predict the impact the changes will have on detector resolution and operation.

II. RAY TRACING FUNDAMENTALS

Every optical system shares a few fundamental components. Light of varying wavelengths enters the device through an aperture, travels through or is reflected by assorted optical elements, and finally either exits the device or, more commonly, strikes a detector where it is absorbed and recorded. In ray tracing algorithms, the treatment of the light is discrete. Starting points are chosen in the aperture plane, and directions of travel are specified for each. Each ray is then followed through the system, with each element bending the ray in some specific direction depending upon not only the type of surface intersected, but also the location of the intersection, the shape of the element at the intersection, and the physical properties of the element itself. The end of the ray's travel through the system is marked by its intersection with the image plane, the element describing the detector in the system. By tracing hundreds or even thousands of rays from a multitude of aperture points and angles, an image is described at the exit that can be analyzed and viewed much as one would see detector output on a monitor or chart recorder. This approach is suggested by the particle nature of light and is ideally suited to the table-top digital computer because it can easily be applied to any number of rays and angles, up to the limits of the memory available in the system.

A. COORDINATE SYSTEMS AND RAY TRACE INITIALIZATION

1. Coordinate Systems

a. Global Coordinates

The use of a consistent coordinate system to describe the placement and orientation of the system components is crucial for correct simulation. In DART, the aperture may be placed at any location in a normal x-y-z orthogonal system, and it is oriented such that the y-axis is up, the z-axis represents a direction normal to the surface of the aperture in the direction of the ray travel,

with an x-axis satisfying the right-hand axis convention. The aperture is always planar, and is typically placed with its center at the origin of the global system. Subsequent elements are specified by their position and by their rotational orientation in the global system.

b. Local Coordinates

The formulas describing each individual element are derived assuming a coordinate system in which the z-axis points in the direction of incoming rays. The local coordinate system for any element is bound to the surface and is rotated with respect to the global system in order to properly orient the element. The amount of rotation is specified for each element as three Euler angles, so named because of their introduction by that famed scientist in his study of dynamics. In particular DART uses a 2-1-3 rotation in which the first rotation is about the y-axis. The next rotation is about the new x-axis and then the last rotation is about the new z-axis, with each rotation occurring after the previous rotation has been completed. Calling the y angle β, the x angle α and the z angle γ, any set of global coordinates or vectors (x,y,z) may be transformed into local coordinates (z',y',z') by applying the commonly used matrix operation given by

$$\begin{bmatrix} x' \\ y' \\ z' \end{bmatrix} = \begin{bmatrix} \cos\alpha\cos\gamma + \sin\alpha\sin\beta\sin\gamma & -\cos\beta\sin\gamma & -\sin\alpha\cos\gamma + \cos\alpha\sin\beta\sin\gamma \\ \cos\alpha\sin\gamma - \sin\alpha\sin\beta\cos\gamma & \cos\beta\cos\gamma & -\sin\alpha\sin\gamma - \cos\alpha\sin\beta\cos\gamma \\ \sin\alpha\cos\beta & \sin\beta & \cos\alpha\cos\beta \end{bmatrix} \bullet \begin{bmatrix} x \\ y \\ z \end{bmatrix} \quad (1)$$

2. Direction Cosines

After making the determination of the location of the ray in both the global and local systems, it is equally important to specify the direction the ray will travel. This is achieved through the use of direction cosines. A direction cosine is defined by the cosine of an angle subtended by the path line from an axis of interest in a plane in which both the line and the axis lie. The direction of travel can be exactly described by using three values, one for each of the three orthogonal axes of the coordinate system. Directions cosines are very convenient because just as position can be converted, a set of direction cosines in the global system (k,l,m) can be converted to direction cosines in the local coordinate system (k',l',m') using Equation (1) .

3. Aperture Ray Generation

Since each ray is treated individually and combined with the other rays to form an image only at the end of the process, the first step is to choose the starting point and direction of each ray in the aperture. The input parameters for the system give the height and width of the aperture in the global coordinate system, centered about the specified position of the aperture center. A number of points across the aperture are specified along with the angular characteristics of each point. The point on the aperture can send rays in a variety of directions, so input of the angular spread about some central angle is allowed, with the number of angular subdivisions in the spread also specified. This scheme allows for very flexible specification of input to the system, since any point on the aperture can be specified with rays emanating at any desired angle. For each point and each angle six parameters are calculated to characterize the ray, which are the three position coordinates and the three direction cosines defining the ray. Once the ray has been defined in the aperture, it is defined, traced, stored and eventually displayed as an output image.

4. General Outline of the Tracing Procedure

For the first element following the aperture, the ray position and directions are transformed into the element's local coordinate system. The intersection of the ray with the element surface is next calculated as shown below. Once the intercept is known the surface characteristics, and in some cases the wavelength of the ray, are used to determine the new direction the ray will travel. The new position and direction are transformed back to the global system and the next element is called to continue the trace. This process repeats for as many elements as given until the ray reaches the last element, where the surface intersection point is saved for later display. The next aperture ray is chosen and the algorithm loops until all of the aperture rays have been traced and stored. With all of the detector intersection data stored, it is a simple matter to compile the individual points into a display of the output image, which is necessarily comprised of many such points. The most difficult task is by far the computation of the ray intersection and the new

direction for the ray at each element. For arbitrary surfaces iterative techniques can in most cases find the intersection, but for simple surfaces the derivation of closed form solutions is possible and saves much computational time.

B. ELEMENT ANALYSIS

This treatment of the element analysis assumes that the position and direction of the ray have already been transformed into the local coordinate system of the element, and shows the steps necessary to produce an element intersection and an associated set of direction cosines that can then be transformed into the local system of the following element.

1. The Most General Intercept Solution

In the local coordinate system, each ray emanates from a point (x_0,y_0,z_0) with a direction cosine (k,l,m) signifying the direction of motion. In this discussion, lower case indicates a ray position, uppercase indicates a point on the element surface, and upper case with a subscript denotes a point on the surface where a ray intersects the surface. If s is the distance the ray will travel from the starting point to the intersection, then the intercept point (X_i,Y_i,Z_i) can be found using three parametric equations

$$X_i = x_0 + ks \qquad (2)$$
$$Y_i = y_0 + ls \qquad (3)$$
$$Z_i = z_0 + ms \qquad (4)$$

The difficulty lies in the determination of the value s. This value is the key to the solution and is a fundamental parameter in interference calculations, as shown below. First find the intersection of the ray with the plane z=0. Calling the distance to this plane s_0 and the planar intercepts X_1 and Y_1 yields

$$s_0 = \frac{-z_0}{m} \qquad (5)$$
$$X_1 = x_0 + ks_0 \qquad (6)$$
$$Y_1 = y_0 + ls_0 \qquad (7)$$

The surface intercept can now be described through substitution of Equations (5)-(7) into Equations (2)-(4) to produce Equations (8)-(10) with the assumption that s is now the distance from the z=0 plane to the surface.

$$X_i = X_1 + ks \qquad (8)$$
$$Y_i = Y_1 + ls \qquad (9)$$
$$Z_i = ms \qquad (10)$$

Every surface used in this procedure must be characterized by an equation of the form F(X,Y,Z)=0. By substitution an equation of one unknown in s is formed that can then be solved by an assortment of techniques. For most planar, spherical or other common geometric shapes this solution can be found directly, and some of these solutions are presented below. Simple closed-form solutions are available for the majority of optical elements in common use, but one of the strengths of this method is that a solution can be found through iterative techniques for any surface free of discontinuities in the region of the intersection. When outlining these steps, Spencer and Murty (1962) suggested that the Newton-Raphson iteration technique would be sufficient to resolve the solution for most cases, but noted that in certain circumstances a solution would not be found. Specifically, if the ray intersects with grazing incidence or if the surface is nonspherical a solution may not emerge. Of course if the ray fails to intersect no solution is possible.

2. Intercepts for Special Cases

For common geometric elements like planes, spheres, ellipses and so forth it is more convenient to derive intersection formulae using Equations (2)-(4), principally because the solution is not iterative and because the value of s is found directly without further calculation. For each case, Equations (2)-(4) are substituted directly into F(X,Y,Z)=0 and solved for $s=s(x_0,y_0,z_0,k,l,m)$. Once the value of s is known, it is a simple matter to calculate the intercept using Equations (2)-(4). The formulae for calculating the value of s for the common types of optical elements are presented in the following sections.

a. Planar Elements

For any planar element, Z=0 in the local coordinate system, so

$$s = \frac{-z_0}{m} \qquad (11)$$

b. Spherical Elements

For a spherical element, it is most desirable to place the sphere such that the origin lies on the surface of the sphere rather than at the center and since the z-axis points in the direction of incoming rays, the sphere is centered on the z-axis at a distance equal to the sphere radius, R.

$$X^2 + Y^2 + (Z - R)^2 = R^2 \qquad (12)$$

By substitution and simplification a simple quadratic form for the sphere intercept is acquired with the normal quadratic constants defined below. In solving for the intercept with a sphere, two intercepts are possible in general. The first intercept of the ray with a sphere will be at a convex surface. After entering the sphere, the ray must exit at a concave surface. To solve for the correct intercept, the proper sign must be chosen in Equation (15): for the concave intercept a + sign is used, and the - sign is used for the convex intercept.

$$b = 2kx_0 + 2ly_0 + 2m(z_0 - R) \qquad (13)$$

$$c = x_0^2 + y_0^2 + z_0^2 - 2z_0R \qquad (14)$$

$$s = -b \pm 2\sqrt{\frac{b^2}{4} - c} \qquad (15)$$

DART checks for the z-axis direction cosine to determine the sign required. If m is negative, the concave intercept is found since it is the intercept closest to the element origin. Similarly, if m is positive, the convex intercept is found to again solve for the intercept closest to the origin. In this way, the spherical model solves only for solutions in the hemisphere on which the origin lies. By translating the spherical element in the global system, this hemisphere can be placed to suit any requirement.

c. Cylindrical Elements

The cylindrical element solution is similar to that of the spherical element. The origin is located on the edge of the cylinder and the cylinder is aligned with its axis parallel to the y-axis. The formula for a cylinder of radius R is then

$$X^2 + (Z - R)^2 = R^2 \qquad (16)$$

As with the sphere, substitutions yield a quadratic solution s, and the treatment of the sign convention to find intercepts is again the same.

$$a = k^2 + m^2 \qquad (17)$$

$$b = 2kx_0 + 2m(z_0 - R) \qquad (18)$$

$$c = x_0^2 + z_0^2 - 2z_0R \qquad (19)$$

$$s = -\frac{b}{2a} \pm \frac{1}{a}\sqrt{\frac{b^2}{4} - c} \qquad (20)$$

d. Eliptical Elements

To specify a three-dimensional elipsoid, the lengths of the major axes must be specified. For simplicity, the axes are aligned in the local system to coincide with the axes of the elipsoid. The elipsoid is also offset along the z-axis such that the origin lies on the elipsoid surface. In the formula for this surface, 2a is the x major axis length, 2b for the y-axis, and 2c for the z-axis.

$$\frac{x^2}{a^2} + \frac{y^2}{b^2} + \frac{(z - c)^2}{c^2} = 1 \qquad (21)$$

As before, s can be found and the correct intercept is found using the appropriate sign convention.

$$A_2 = \frac{c^2}{a^2} \qquad (22)$$

$$B_2 = \frac{c^2}{b^2} \qquad (23)$$

$$A_3 = A_2k^2 + B_2l^2 + m^2 \qquad (24)$$

$$B_3 = A_2kx_0 + B_2ly_0 + m(z_0 - c) \qquad (25)$$

$$C_3 = A_2x_0^2 + B_2y_0^2 + (z_0 - 2c)z_0 \qquad (26)$$

$$s = \frac{-B_3 \pm \sqrt{B_3 - A_3C_3}}{A_3} \qquad (27)$$

e. Parabolic Elements

The parabolas used in DART are centered about the local z-axis and are defined by the focal lengths of the parabola in the z-x and z-y planes. In the z-x plane, the parabaloid creates a planar parabola intersection with a focal point f_x on the z-axis such that $4f_x = a$. Similarly in the z-y plane the intesecting parabola has a focal point f_y on the z-axis such that $4f_y = b$. The formula for the elliptic paraboloid is then

$$\frac{X^2}{a} + \frac{Y^2}{b} = Z \qquad (28)$$

Making the usual substitution results in another quadratic solution for s shown in Equation (32), subject to the same conventions for intercept selections. Note that for a paraboloid with a ray moving in the -z direction a concave solution will always exist, but a convex solution may not. The reverse is true when the ray is moving in the +z direction. By keeping the sign convention used for the other elements when solving the quadratic, the solution closest to the origin is always found, and the other potentially imaginary intersect is ignored. A parabolic trough can obviously be specified if a or b is large enough to significantly reduce the x or y dependence in the formula.

$$A = \frac{k^2}{a} + \frac{l^2}{b} \qquad (29)$$

$$B = \frac{kx_0}{a} + \frac{ly_0}{b} - \frac{m}{2} \qquad (30)$$

$$C = \frac{x_0^2}{a} + \frac{y_0^2}{b} - z_0 \qquad (31)$$

$$s = \frac{1}{A}\left[-B \pm \sqrt{B^2 - AC}\right] \qquad (32)$$

3. Factors Needed To Find Direction Changes After Intersection

The directon the ray takes after intersection is as important for continuing the trace as the point of intersection found above, and requires more computation. Fundamental in the solution for the new direction cosines (DC) is **r** = (K,L,M), the vector normal to the surface at the point of

intersection. Since F(X,Y,Z) is known for an element, the normal vectors are found through the calculation of the partial derivatives at the surface intersection

$$K = \frac{\partial F}{\partial x}\Big)_i \qquad L = \frac{\partial F}{\partial y}\Big)_i \qquad M = \frac{\partial F}{\partial Z}\Big)_i \tag{33}$$

Spencer and Murty (1962) outline the steps necessary to determine the new DC in the case of refractive index change, reflection and refraction. For the first, the value μ must be known, equal to the ratio of the incident index of refraction to the exiting index of refraction. Reflection results are found as a subset of the refraction case in which the value of μ is assumed to be unity and the signs of the DC are chosen appropriately. For diffraction the terms specific to a grating surface must be introduced. With these data, a solution for the new DC can be calculated.

4. The Most General Direction Cosine Solutions

These solutions are a restatement of the methods described by Spencer and Murty (1962) and use similar nomenclature for consistency. Included here are key points in the development of the working ray trace algorithm.

a. Refraction

The new DC is described by **S'** = (k',l',m'). The vector form of Snell's Law can be resolved through a few substitutions to yield a quadratic equation, which when solved yields the new DC.

$$\text{Snell's Law} \qquad \mathbf{S'} \times \mathbf{r} = \mu \mathbf{S} \times \mathbf{r} \tag{34}$$
$$\mathbf{S'} = \mu \mathbf{S} + \Gamma \mathbf{r}$$

Γ is the multiplier that will be solved quadratically. The three components of (34) are

$$k' = \mu k + \Gamma K, \quad l' = \mu l + \Gamma L, \quad m' = \mu m + \Gamma M \tag{35}$$

Since the sum of the squares of the DC components equal one, Γ can be found

$$\Gamma^2 + 2a\Gamma + b = 0 \qquad (36)$$

where $$a = \mu\left(\frac{kK + lL + mM}{K^2 + L^2 + M^2}\right) \qquad (37)$$

and $$b = \left(\frac{\mu^2 - 1}{K^2 + L^2 + M^2}\right) \qquad (38)$$

Γ can be solved by any variety of techniques, and a solution via the quadratic equation is usually satisfactory. Once Γ has been found, substitution into Equation (35) produces the new DC, which satisfies the definition of a unit vector.

b. Reflection

The equations for the refraction case provide the reflection solution directly. In the quadratic formula solution, the addition of the square root term signifies the reflection case and the root subtraction signifies the transmission case. Since for most mirrors μ=1, then b=0 and a direct solution is then available for Γ

$$\Gamma = -2a \qquad (39)$$

c. Grating Characteristics

Gratings present the most challenging computational task. In addition to the variables needed to define other elements, gratings require a specification of the number of rulings per unit length, the order of the path to be traced, the wavelength of the incident ray and the vector **p**=(u,v,w) describing the direction normal to the ruling surface, all at the point of intersection. The ruling normal vector, **p**, is found for two cases by Spencer and Murty.

1) Case I: *Parallel Rulings*. Parallel rulings are formed by the intersection of a surface with parallel planes. Since DART allows an element to be rotated in the global system, it is perfectly general to assume that the lines of intersection run parallel to the y-axis. The plane spacing d is usually a constant, but may be any function of x. It can be shown that the components of **p** and the local spacing d are

$$u = \left(1 + \frac{K^2}{L^2 + M^2}\right)^{-\frac{1}{2}} \tag{40}$$

$$v = 0 \tag{41}$$

$$w = -\frac{KMu}{L^2 + M^2} \tag{42}$$

$$d = \frac{f(x)}{u} \tag{43}$$

2) Case II: *Circular rulings*. Circular rulings are formed by the intersection of concentric cylinders, lying along the z-axis, with the surface. In this case d is a function of the distance ρ from the center, and the resultant equations for **p** and d are

$$G = \sqrt{\left(K^2 + L^2 + M^2\right)\left[M^2\rho^2 + \left(LX_i - KY_i\right)^2\right]} \tag{44}$$

$$u = \frac{1}{G}\left[M^2X_i + L\left(LX_i - KY_i\right)\right] \tag{45}$$

$$v = \frac{1}{G}\left[M^2Y_i + K\left(LX_i - KY_i\right)\right] \tag{46}$$

$$w = -\frac{M}{G}\left(KX_i + LY_i\right) \tag{47}$$

$$d = \frac{\rho f(\rho)}{X_i u + Y_i v} \tag{48}$$

d. Refraction Solutions for Gratings

With the surface characteristics in hand, a solution of the refracted DC are possible. The diffraction may be represented by

$$\mathbf{S'} \times \mathbf{r} = \mu\mathbf{S} \times \mathbf{r} + \Lambda\mathbf{q} \tag{49}$$

giving $\mathbf{S'} = \mu\mathbf{S} - \Lambda\mathbf{p} + \Gamma\mathbf{r}$ (50)

where $\Lambda = \frac{n\lambda}{N'd}$ (51)

n is the order number, λ is the wavelength, N' is the exiting index of refraction and **q** is the unit vector parallel to the rulings. Note that for the zero order case, (49) reduces to Snell's Law. Equation (50) can be expanded to

$$\begin{aligned} k' &= \mu k - \Lambda u + \Gamma K \\ l' &= \mu l - \Lambda v + \Gamma L \\ m' &= \mu m - \Lambda w + \Gamma M \end{aligned} \tag{52}$$

which once again yields a quadratic equation in Γ with Equation (37) representing a as before. The choice of sign in the solution of the quadratic equation is identical to the reflection case above.

$$\Gamma^2 + 2a\Gamma + b' = 0 \tag{53}$$

$$b' = \frac{m^2 - 1 + \Lambda^2 - 2m\Lambda(ku + lv + mw)}{K^2 + L^2 + M^2} \tag{54}$$

Once the value of Γ is solved, simple substitution into (52) yields the new DC.

5. Direction Cosines in DART

DART uses the above algorithms to determine the new DC. One subroutine could be used to calculate any of the elements in the program, but this approach would take the same amount of time for any surface, regardless of the type. In a quest for enhanced speed performance, each surface type is treated individually with extraneous terms omitted from the calculation and with appropriate term reductions incorporated. In this way extra data are not computed and the computational time for a plane surface is ten times less than that required for an elliptical grating, for example. Furthermore, every element available in DART can be solved without the use of iterative routines, so straightforward quadratic solutions serve to enhance speed even more than what would be possible in the general iterative case. On the other hand, DART is fully expandable and any arbitrary surface can be added to the program if desired.

III. DART MODULES

In addition to the raytracing features incorporated in DART, analysis modules are included to manipulate the output data. DART can store the ray information to user-specified files in text or binary format. It can perform some routine analyses for the user and can transfer data to other programs like word processors or spreadsheets. This section describes the modules implemented in DART.

A. LAYOUT MODULE

DART will draw the system to be analyzed if the user selects the Layout feature from the program menu. The system layout is drawn initially as an isometric projection, but the user can set the viewing angle to any desired orientation. After the layout is drawn, any rays that are traced with the program are drawn on the layout, so that the point of impact on any surface can be seen. Only rays that actually hit a surface within the limits of its mask are drawn. At any time the layout and any rays that are on the layout can be transferred to a word processor or spreadsheet program for editing or annotation. Figures 1 and 2 show the isometric and x-z plane views of the MUSTANG instrument.

B. DATA STORAGE MODULES

Data storage is a primary concern in table-top programming. Each ray must be stored so that after all of the rays are traced they can be recalled to build an image for display. The reading and writing of data to the fixed disk drive is the slowest operation in the process and is the determining factor in the time required to trace a system. To keep the bytes of data to a minimum, each number is stored using a binary format with ten bytes per number. Ten bytes are used instead of eight or four so that the precision of the answer will be as high as the PC math processor will allow.

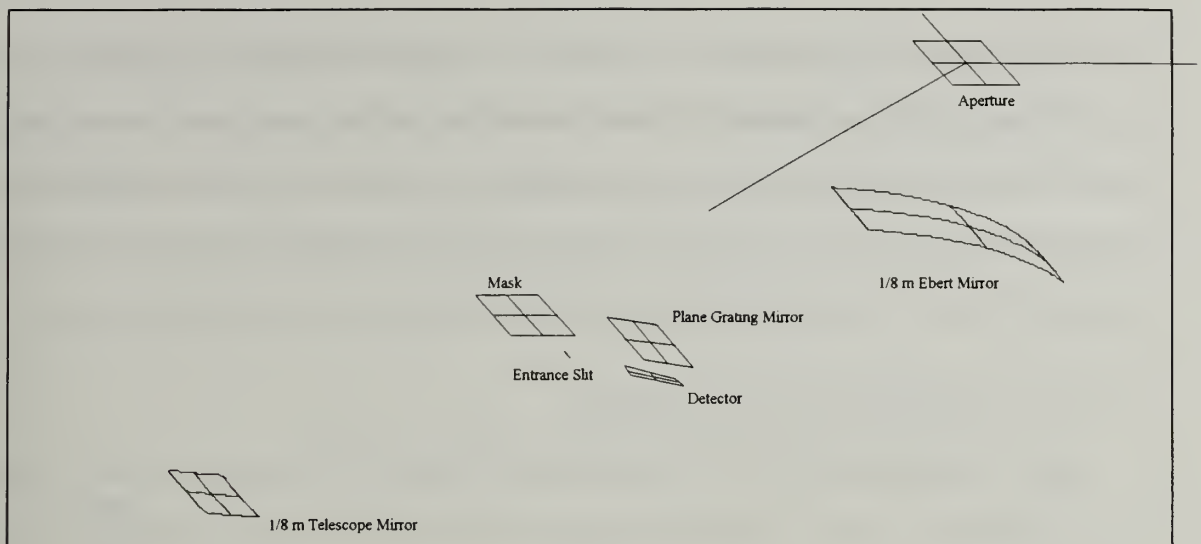


Figure 1. MUSTANG Layout Using Isometric View. The X-axis is to the right, Y is up and Z is to the left. The aperture is shown by the square at the origin, and rays will travel from the aperture along the z-axis.

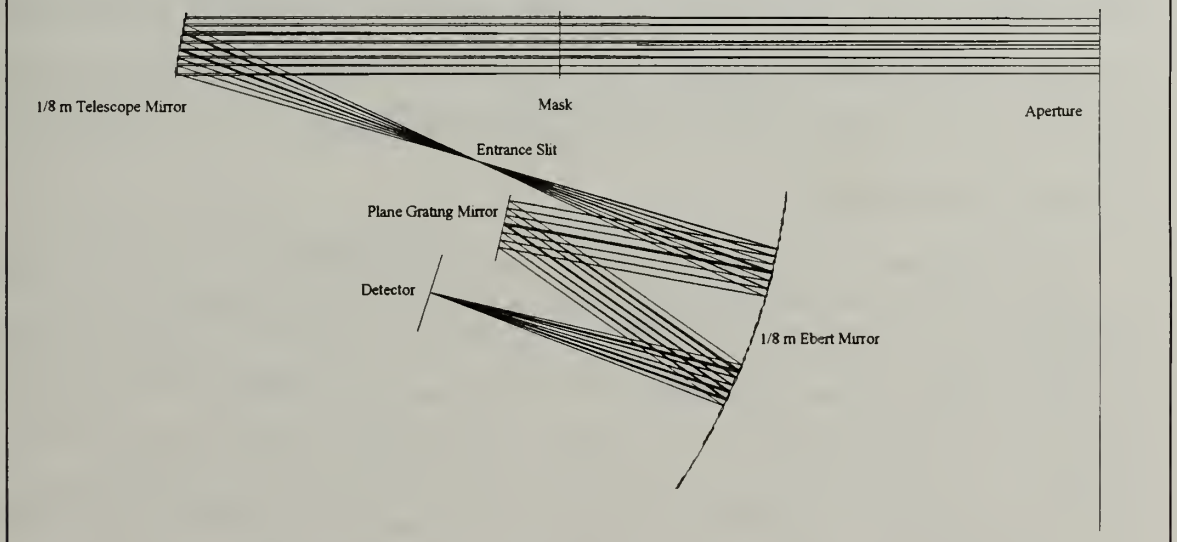


Figure 2. MUSTANG Top View of X-Z Plane. In this view the X-axis runs down while the Z-axis goes to the left of the aperture, where the rays enter the system. The beam focuses onto the surface of the CCD detector and is a function of wavelength.

Binary storage is much better than text storage with one byte per character in the written number, but if the user wants to inspect the data with a printout or a text file, binary format is unintelligible. For this reason all of the ray tracing is done using binary storage, but data storage to disk after the tracing is complete can be in either binary or text format. The output image can also be saved to disk as a bitmap file for later manipulation, editing and printout.

C. FULL WIDTH AT HALF MAXIMUM

When analyzing the MUSTANG instrument (see Chapter IV), a parameter of primary focus was the detector resolution. Resolution describes the ability of the device to discriminate between different received wavelengths, and is measured as the wavelength difference required to distinguish two adjacent lines. In a system that contains gratings, the position of the output image is a function of wavelength. This is true in the MUSTANG, where the position on the detector maps directly to the wavelength of the light entering the system. Monochromatic light entering the system with a wavelength between 1800 and 3400 Å makes a line on the detector. Since the lines have a finite width and a central maximum, there exists a point on either side of the maximum where the received intensity is one-half of the maximum; the distance from one half-point to the other is the Full Width at Half Maximum (FWHM). The FWHM is used to determine the resolution of the instrument.

DART computes the FWHM for any output, along either the detector x or y axis. For this explanation, we will assume that the FWHM along the x-axis is desired. In this case the user specifies the minimum and maximum x values for the detector size and the number of bins in the detector. The data are arranged into a histogram similar to the one shown in Figure 3. The FWHM routine then uses the value of the maximum bin to locate the two bins nearest one-half the maximum. Interpolation provides the x-coordinate of the halfway points, and the distance between these points is the FWHM. This value is immediately displayed to the user.

Unfortunately, the FWHM routine is not inerrant since the bin width (defined by the number of the bins and the range of analysis) will directly affect the interpolated result. Because of this the routine also dumps the bin values to a text file that can be used in a spreadsheet to plot the number of hits versus position as shown in Figure 3. This allows the user to measure the FWHM by hand and to account for irregularities in the plot with any unique method desired.

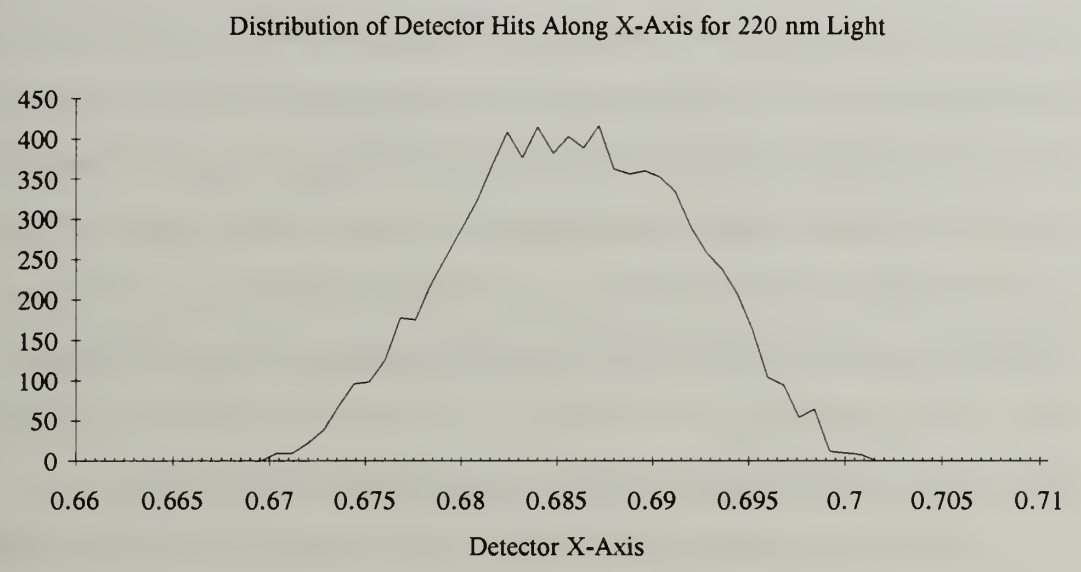


Figure 3. Example Plot of FWHM Curve

D. INTERFERENCE MODULE

A next-generation interferometer being designed at NPS will use interference patterns to achieve resolution enhancements at least three, and perhaps four orders of magnitude higher than possible with the MUSTANG instrument. Construction of these interference patterns is one of the fundamental features of DART and was one of the primary reasons for its development. Excellent treatments of interference properties are provided in a number of texts, including Hecht (1990) and Jenkins & White (1976) and will not be reintroduced here; only the facets of interference pertaining to its use in DART will be covered.

1. Key Ideas For Interference Computation

Huygen's principle states that each point on a wavefront acts as an unique point source, and that through superposition of waves from an infinite number of point sources along the front, the wave is propagated forward. If some medium is introduced between a source and a target, it is possible to prevent some or all of these secondary wavefronts from arriving at the target, resulting in a waveform that is not the same as the original. The light intensity at a point on a target will depend upon the number of wavefront sources blocked by the medium and upon the location of the blockage. In particular, the target intensity will be a superposition of the rays coming from each point on the wavefront. If the phase of the light from different sources varies (phase is dependent upon the pathlength traveled) then it is possible that constructive or destructive interference will occur at points on the target and patterns of interference may be developed. At the edges of a beam this interference effect is called *diffraction*, and is the result of path length differences within the beam. *Interference* occurs in cases where two or more beams are formed from a single source and subsequently recombined in such a way that the components of the beams interfere.

Interference is generally created through two mechanisms: wavefront splitting and amplitude splitting. In wavefront splitting, portions of the original wavefront are used to create secondary wavefronts that interfere. In amplitude splitting, the whole wavefront is divided into multiple segments that then travel different path lengths before recombining with interference. This thesis investigates the simulation of interference patterns caused by amplitude splitting devices like the Michelson interferometer. In the Michelson interferometer, a partially-silvered mirror reflects half of the incident light, and passes the rest. Each beam then travels a different length before being returning to the half-silvered mirror, where the beams recombine. The recombined beam then travels to a detector where the interference is measured as a variation of intensity across the detector.

Ideally, an infinite number of points exist on a wavefront, and each point is a source for another infinite number of rays. A solution involving an infinite number of rays is not practical, but DART uses a discrete method to superimpose the effects of various paths to generate an interference pattern for the user. A word of caution is in order since DART is not a real physical system. It is easy to create input scenarios that will generate interference patterns in DART, but that cannot possibly work in practice. One example would be to run rays from the aperture directly to a detector some distance away from the aperture. If the detector were rotated some small angle and the output compared for interference with the first case, fringes would be calculated by the algorithm because the path lengths would be different as the distance from the axis of rotation was increased, but in reality no interference is possible. The user must ensure that the model to be simulated is actually capable of generating interference. There are other limitations to the construction of interference patterns in DART, and these will be treated after the algorithm is presented.

DART was designed to handle interference patterns resulting from two different paths of light, like the patterns produced by Young's experiment or by the Michelson interferometer. For interference to occur in practice, a ray should start at some common point and be subsequently split into two paths. Somewhere else in the system the split rays recombine and travel toward the detector. An interference effect occurs when the rays recombine if the phases of the recombining rays are different and in general, interference will be created at the detector if the split rays fall at or near the same point on the detector. To simulate an interferometer with DART, it is necessary to run two systems, each system representing one of the two possible paths in the interferometer. For the split paths the aperture data should be identical, with one or several elements in the system altered to produce a different path that creates interference. Prior to the start of the interference module, the user should have saved the ray-trace data from each of the optical paths in separate

data files. In these files three values are stored for every ray that hits the detector: the x-coordinate, the y-coordinate and the length of the path traveled from the aperture to the target.

2. The Interference Algorithm

The user must specify the size of the interference pattern on a screen of a certain width and height. This screen is sectioned into a large number of bins of small area which are used to sum interference hits for the final image. Two data files are specified for use in constructing the interference pattern, each file containing one of the two paths previously traced for the optical device causing interference. The data files contain the results of the two individual paths in the system where the aperture points for each are the same. The interference algorithm takes one datum point from each file, determines if interference has occured, and increments the correct detector bin as appropriate. Since the routine loops until all of the data points in the files have been tested, a description of the analysis for one set of points is sufficient to demonstrate the computational principle.

Data for the first ray are taken from file 1 as x1, y1 and L1. The data for the interfering ray are taken from file 2 as x2, y2, L2. If ray one and ray two fall in the same bin, then their interference is calculated as

$$\text{Value} = 4\left\{\cos^2\left[\frac{2\pi}{\lambda}(L1 - L2)\right]\right\} \qquad (55)$$

If the rays have a pathlength differing by a multiple of the wavelength λ, then they constructively interfere and 4 is added to the value of the appropriate bin. If they vary by exactly one-half λ, they destructively interfere and nothing is added to the bin value. If the rays do not fall in the same bin, then each of the two bins are simply incremented by one to signify a hit of a ray.

DART also provides an imaging enhancement to remove some of the visual effects caused by the discrete nature of the rays. Since any ray can hit in only one bin (pixel), many pixels may not contain ray hits. These pixels will stand out in sharp contrast to the neighboring pixels which

will show hits. At the same time, some bins will show no hits when in fact hits did occur that resulted in destructive interference. To smooth these effects a box filter is applied, in which every bin is calculated as the average of the hits in that bin and the hits in all neighboring bins. This technique tends to smooth out the rough edges from discretization while retaining the highs and lows of interference. The user has the option to engage this filter or to ignore it.

3. Limitations of the Interference Routine

DART calculates the interference resulting from a pair of beams split somewhere in the optical path. Systems utilizing multiple-path interference, i.e., Fabry-Perot interferometers, cannot be modeled because DART cannot synthesize the very large number of interfering rays. The program would need significant alteration before these systems could be accomodated.

The interference pattern displayed to the user depends upon the number of pixels available to the image. When the user sets the size of the image, a fixed number of pixels are available to show that image. If the number of rays is small compared to the number of pixels, the resultant "hits" may be spread out so far that recognition of an interference pattern is difficult or impossible. Conversely, if the number of pixels available is very small, which occurs when the size of the given detector is much larger than the image, the rays may saturate a few pixels and not generate a distinguishable pattern. A pattern also will not be recognizable if the high and low intensity points of the pattern are separated by a distance less than a few pixels, simply because the resolution of the display will not show any difference between the two points. These resolution pitfalls can be circumvented by the user through a thoughtful choice of image size and ray density.

Another striking effect is caused by the process of stepping in a linear fashion through the aperture points to get new rays for tracing. This means that all of the rays in the aperture are equally spaced according to the input specification. Since the detector intercept points for a linearly stepped aperture also tend to be linearly stepped, moiré patterns are developed that run the length of the output image. Because interference is recognized in the display as differences in the

pixel intensity across the image, the moiré pattern could be misinterpreted as interference in the output where in fact none may exist. To avoid this problem, the user may select a scattered aperture input set. The way this works is that after each linear step to the next aperture point or angle, a small offset is added using a pseudorandom number supplied by the computer's random number generator. In this manner the output pattern is randomized and the output moiré patterns are destroyed. The random nature of the image allows the user to recognize anomalies as part of the analyzed system, and to have faith that the display itself is not the cause of the pattern.

IV. ANALYSIS OF THE MUSTANG

The NPS MUSTANG is an instrument used to passively measure emissions from ionospheric atomic and molecular species. This thesis uses the MUSTANG as a benchmark for model verification, since the resolution, frequency response and field-of-view specifications for the instrument are well-known (Anderson, 1990; Chase, 1992). It was also analyzed for significant design changes that are being made for a slated satellite deployment in early 1995.

A. DESCRIPTION OF MUSTANG

The MUSTANG (Middle Ultraviolet SpecTrographic Analysis of Nitrogen Gasses) instrument has twice been successfully launched using Black Brant, Terrier boosted sounding rockets at the White Sands Missile Range in conjunction with the Naval Research Laboratory and NASA. The purpose of the experiment is to study the emissions of atomic and molecular species naturally present in the ionosphere so that the processes governing their creation and concentration can be modeled and eventually predicted. If the ionosphere can be accurately predicted, many systems can be developed in communications and surveillance areas to take advantage of the interaction between electromagnetic phenomena and the atmosphere.

Figure 4 shows the optical layout of the MUSTANG. Light enters the aperture of the device and travels through the telescope section to a spherical mirror with a 1/8-meter focal length. Baffles in the telescope assembly stop light that would otherwise reflect from the inner surfaces of the telescope. The mirror focuses the light such that the beam is narrowest at the entrance slit, which cuts off the edges of the beam and acts to restrict the field-of-view of the instrument even more than the baffles do. A smaller slit in general yields a smaller field-of-view but at the same time it reduces the amount of light that reaches the detector. If the field-of-view is constrained too much, the small amount of light that hits the detector may be unmeasurable. As the reflected light

expands after passing the slit it strikes the second 1/8-meter mirror which collimates the beam and redirects it onto the plane grating. The first order grating reflection is again reflected by the 1/8-meter spherical mirror and is focused to strike the linear array photodiode detector where the light is collected. In the MUSTANG, the grating is ruled at 1200 lines/mm so that a band of wavelengths 1600 Å wide will strike the active portion of the detector. The detector can collect a beam 2.5 cm wide and 0.5 cm high with 512 bins along the wide dimension. The grating is rotated so that the rays hitting the detector correspond to a low wavelength of 1800 Å at the top of the detector and to a high wavelength of 3400 Å at the lower side of the detector. The received photon intensity at each bin is electronically converted to a proportional signal that can then be transferred by the rocket telemetry system to a recorder that in real time stores the information generated by the instrument. In this way continuous ionospheric emission data can be obtained for a fifteen minute flight to a peak altitude of about 320 km, with the time of receipt directly correlatable to the altitude of the measurement.

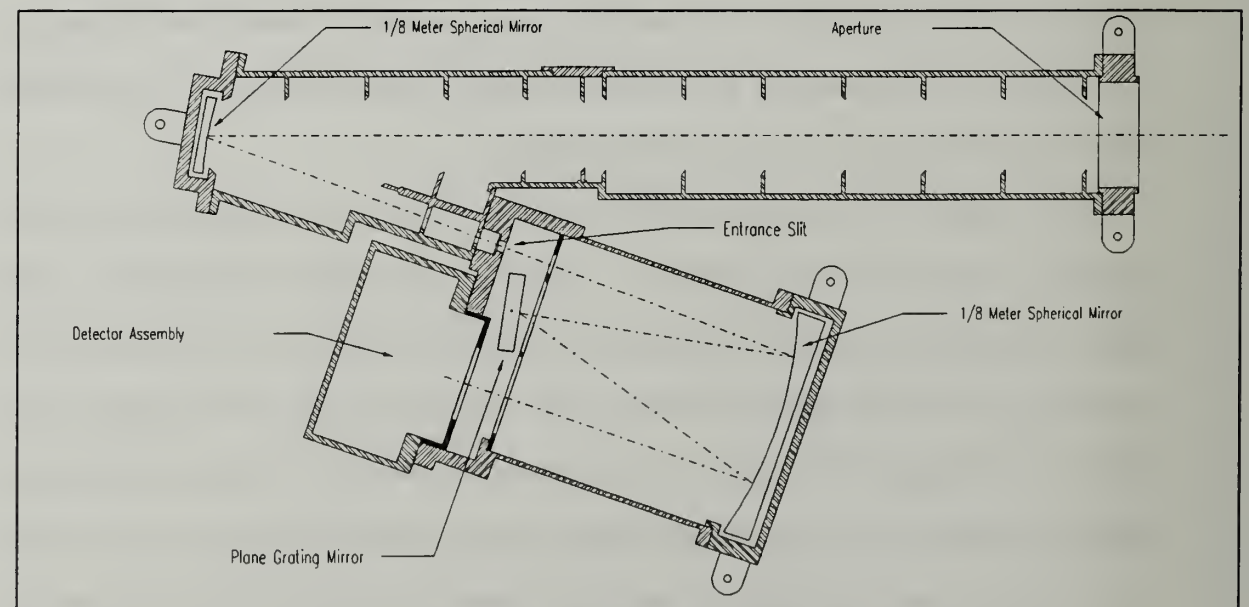


Figure 4. MUSTANG Instrument

Other students are analyzing the data generated by the previous two launches. This thesis uses the MUSTANG as a yardstick against which DART can be measured. The calibration of the MUSTANG yielded values of system performance that included the field-of-view of the device, the resolution of the detector, and the wavelength calibration. DART independently calculates all of the parameters.

B. ANALYTICAL RESULTS

1. Line Placement

Gratings will reflect light in several directions, with the diffraction angle dependent upon the wavelength of the incident light, the ruling density and the ruling direction. This property is fundamental to the action of the MUSTANG, which is tuned so that only light in a fixed range of wavelengths will be properly reflected to hit the detector, and also so that the wavelength received can be directly mapped to the physical location of the receiving bin. Table 1 shows the element data used for the analysis of the MUSTANG properties in the order in which the light strikes the objects. The aperture was specified as a square centered about the origin with width and height of 2.66 cm; the positive Z-axis is normal to the center of the aperture.

Table 1. MUSTANG ELEMENT PLACEMENT IN ORDER OF IMPACT

	Position of Center (cm)			Rotation Angles (deg.)			Mask Info (cm)	
Type	X	Y	Z	X	Y	Z	Width	Height
Telescope Mask	0.000	0.000	21.194	0.000	0.000	0.000	2.500	2.500
Spherical Mirror	0.000	0.000	36.195	0.000	169.855	0.000	2.500	2.500
Entrance Slit	4.335	0.000	24.471	0.000	-18.872	0.000	0.014	0.500
Ebert Mirror	11.288	0.000	13.713	0.000	-21.393	0.000	12.000	2.500
Plane Grating	6.795	0.000	23.479	0.000	167.500	0.000	2.500	2.500
Ebert Mirror	11.288	0.000	13.713	0.000	-21.393	0.000	12.000	2.500
Detector Surface	9.271	0.000	26.340	0.000	161.128	0.000	3.000	0.500

The measurements of Table 1 are made with a few coordinate system assumptions. Referring back to Figure 2, the center line of the telescope section is taken as the Z-axis, with

travel to the left indicating a positive direction. The X-axis is chosen down, so that in a right handed convention the Y-axis is out of the page. The origin is placed at the intersection of the aperture plane with the Z-axis, and all angles are measured so that a positive rotation executes a right handed turn about an axis. Each wavelength creates a separate line at the detector because the grating is ruled in the Y-direction, such that reflection is a function of wavelength in the X-Z plane but not in the Y-direction; any ray moved vertically remains unaffected by the grating. Figure 5 shows the line produced by a 2600 Å source.

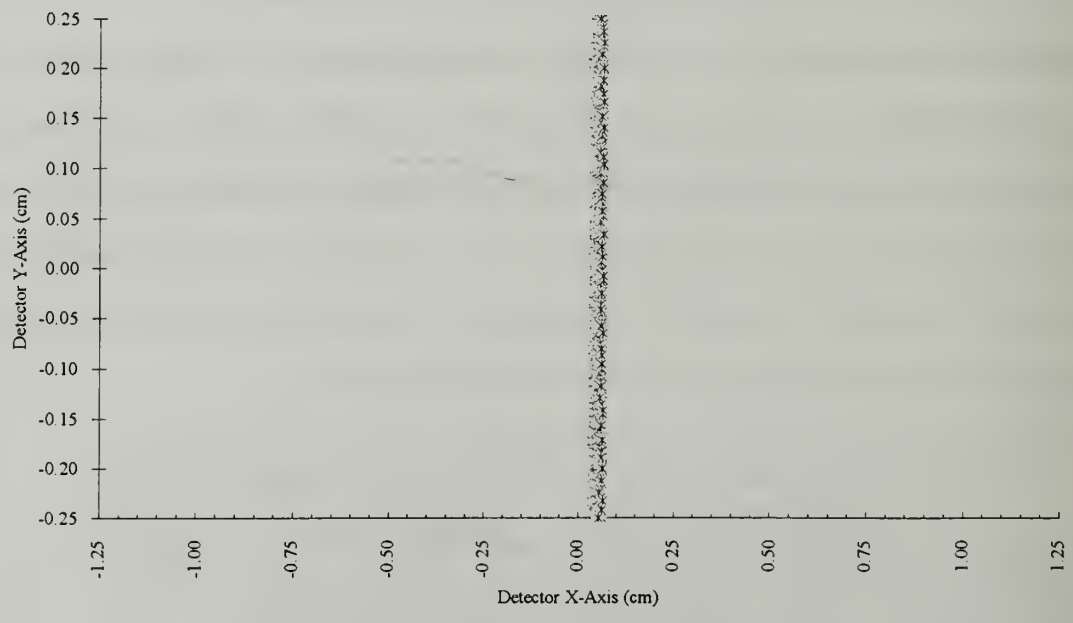


Figure 5. MUSTANG 2600 Å Line by DART Analysis

The grating element is mounted so that it can be rotated about its Y-axis, allowing the lines created on the detector to be moved from one location to another simply by turning the grating a small amount. The values of Table 1 were used by DART along with the physical characteristics of the grating and spherical mirrors to find where various wavelength sources would strike the detector. Using the left and right bounds of the output image as the limits of the line, the FWHM

module was used with 100 bins along the X-axis to create a FWHM plot like Figure 1. The maximum point was estimated and from this the half-maximum value was determined. The center of the line along the X-axis was taken as the midpoint between the two half-maximum points. Figure 6 is the result of this analysis for nine different wavelengths.

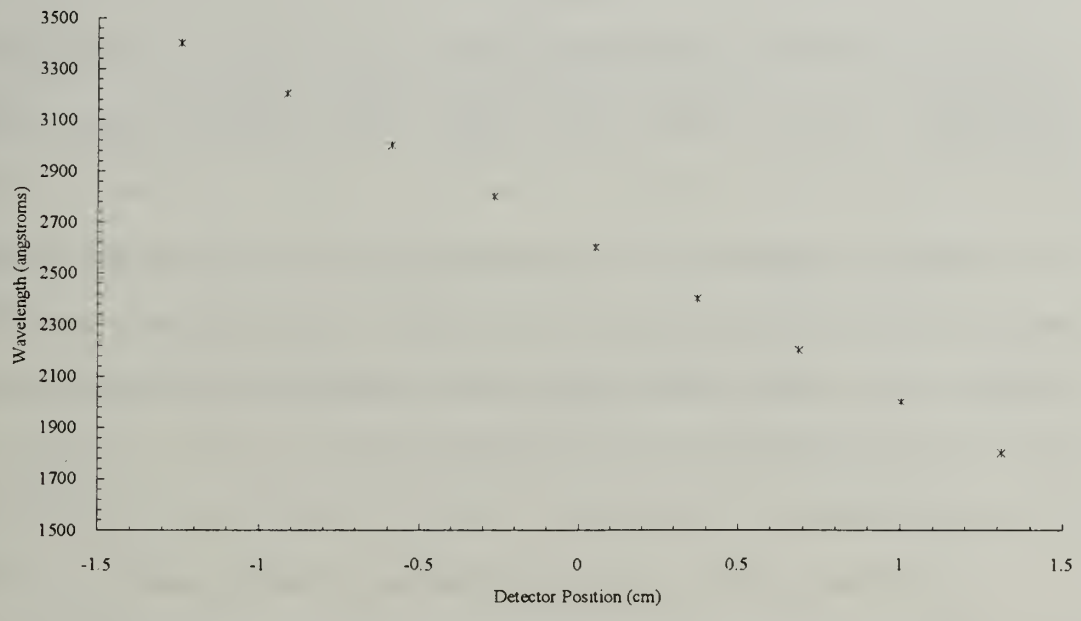


Figure 6. MUSTANG Line Placement For Varying Wavelengths

The linear response shown in Figure 6 is due to the linear ruling density on the grating and the small difference between the wavelengths in the range of interest. It matches the line placement that was measured by Anderson (1990).

2. Detector Resolution

Another parameter of great interest is the resolution of the detector. Resolution in this application is defined as the wavelength difference required to clearly differentiate between adjacent lines on the detector, and is found as the wavelength separation such that the FWHM points of adjacent lines just overlap. To determine the resolution of the detector optics, the line

data for some representative cases was plotted as a FWHM curve as done for the previous case of the center determination. The wavelength dispersion was calculated using the difference between the maximum and minimum wavelengths divided by the separation between the minimum and maximum X-axis intercepts. This value was multiplied by the FWHM distance for each individual wavelength to produce the resolution value at that wavelength. Table 2 lists the resolution results.

Table 2. MUSTANG LINE RESOLUTION AS A FUNCTION OF WAVELENGTH

Wavelength (Å)	1800	2000	2200	2400	2600	2800	3000	3200	3400
Resolution (Å)	10.0	10.0	9.9	10.3	10.0	10.2	10.4	10.3	10.2

The slight variation in resolution with wavelength derives from the discontinuous nature of the FWHM plot from which the linewidth data is taken. The key result is that the MUSTANG resolution over the range of interest is approximately 10 angstroms, which is very close to the 10.6 Å value determined experimentally by Anderson (1990).

3. Field-of-View

The field-of-view of the instrument describes how far from the principal axis the light source may be while still producing an image on the detector. This parameter is critically important for the proper analysis of the experiment data, since the detector measures a portion of all of the light directed toward it in its field-of-view. The field-of-view is needed first for the instrument calibration in the laboratory with a known light source so that the detector response can be established. The field of view is then used with the calibration data for post-experiment analysis of the data.

The field of view for the MUSTANG was determined experimentally along the Y-axis by Anderson (1990). Two methods are possible to compute the field of view using the program: rotate the instrument or move the initial ray source. Moving the instrument in DART would require rotating and correctly translating every element in the system to the new position and would

be very time-consuming and error-prone. It is possible to specify in the program input the exact angle that the aperture rays initially travel, so in this way perfectly collimated rays are injected into the instrument at precisely controlled angles, without any limit set by the resolution of a turntable or micrometer.

For the Y-axis the field-of-view is much larger than that of the X-axis, since the entrance slit is much thinner in X than it is in Y. The Y-axis field of view was tested for angles that ranged from -25 to +25 milliradians. 10,000 rays arranged to uniformly fill the aperture and with a direction normal to the aperture plane were input to the program, causing 5173 rays to hit the detector. To determine the field-of-view the angle was repeatedly changed and the number of hits recorded at the new angles. By comparing the number of hits at various angles, the field-of-view can be shown. Figure 9 is a plot of detector hits as a function of incidence angle. This curve is consistent with the experimental determination of Anderson (1990, pg. 53). Anderson found a Y-axis field-of-view of about 35 mrad and estimated an X-axis field-of-view of less than 7 mrad. With DART the Y-axis field-of-view was about 34 mrad and the X-axis field-of-view is about 4 mrad.

Unfortunately, the X-axis field of view was too small to be measured using available laboratory equipment, but it was estimated less than 0.08 degrees (Anderson, 1990). DART can easily solve for extremely small angles, and through the same method applied for the Y-axis case the X-axis field of view is presented as Figure 10. The field of view along the X-axis has a complex shape with a very sharp peak at the center and that decreases much faster in positive angles than in negative angles. This feature is due to the spherical aberration resulting from the use of a tilted spherical mirror to divert the light through the entrance slit. If the field-of-view is taken as the point where the number of hits is one-half of the maximum, the field of view along the X-axis is 0.07 degrees.

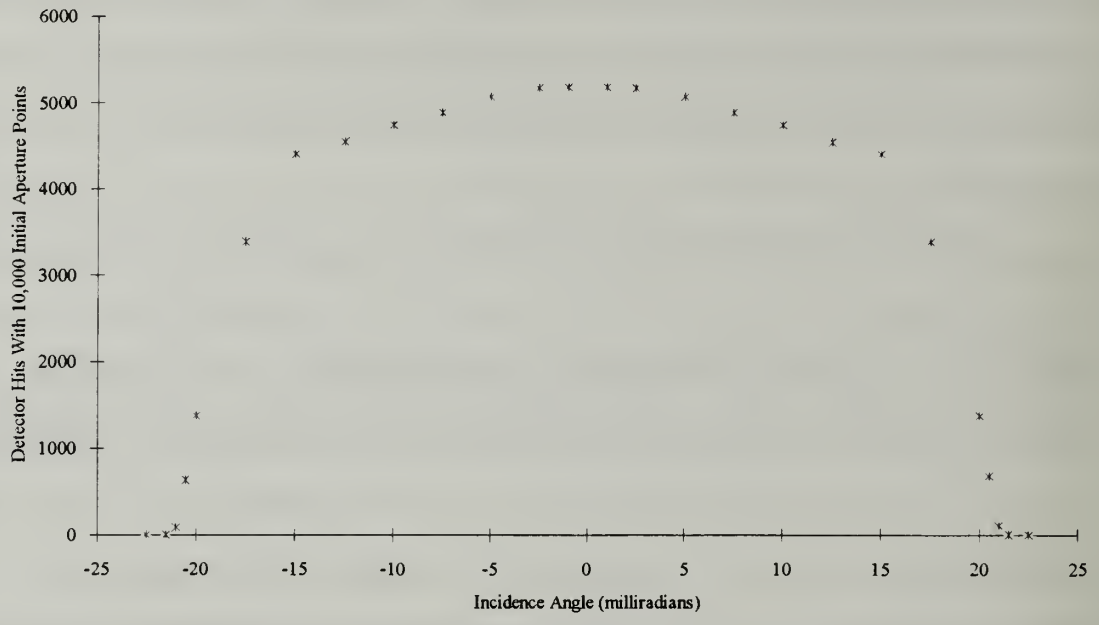


Figure 9. Y-Axis Field of View for MUSTANG

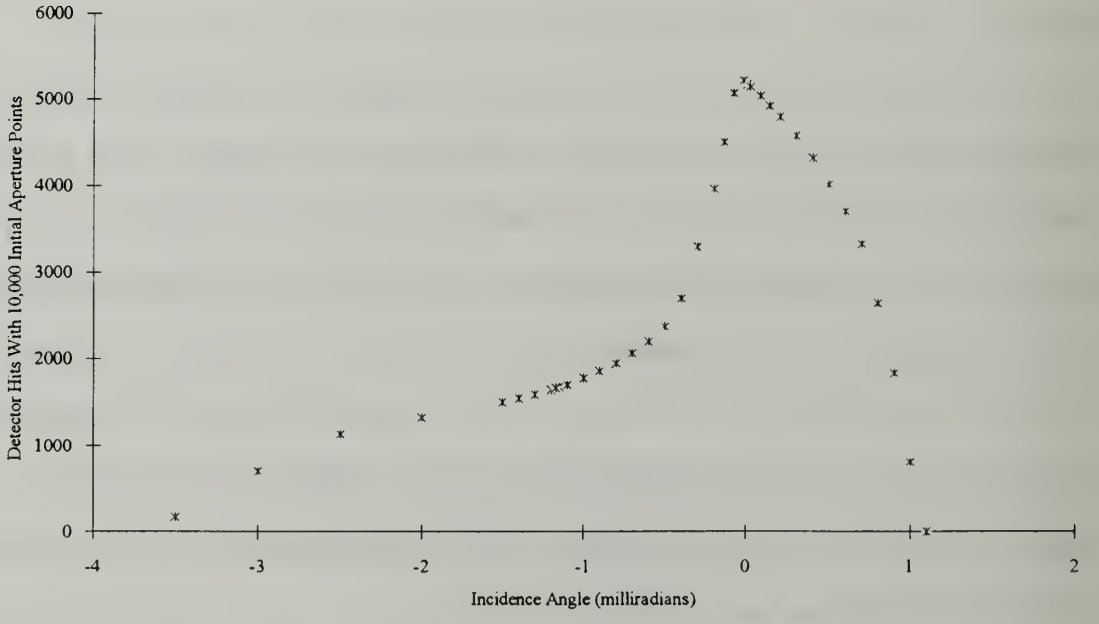


Figure 10. X-Axis Field of View for MUSTANG

V. MUSTANG ON ORBIT (ISAAC)

A new version of the MUSTANG instrument will be placed on orbit sometime in 1995 in order to study the ionosphere for an extended period of time (Cleary, 1992). The satellite that will be used for this experiment is the Air Force sponsored ARGOS science satellite. The purpose of ARGOS is to carry a number of advanced scientific experiments on orbit for a period of at least one year, and the MUSTANG is an integral part of this project. The current instrument could be modified with the correct telemetry electronics to support the satellite bus requirements, but since the experiment is a long-term project some significant design changes are worthwhile; DART has been used to quantify the effect of these changes. The new instrument will be called ISAAC.

A. DESIGN CHANGES

The first goal of the design change is to enhance the detector resolution. The principal determinants of resolution are line-width and line separation. The first design change was to raise the number of rulings on the grating from 1200 to 4800 lines/mm. This has the effect of splitting the 1800-3400 Å light departing the grating into an angle at least four times larger than before. The next design change seeks to reduce the line-width by narrowing the entrance slit to one-half of the original width. The third change incorporates an off-axis parabolic mirror element to replace the spherical mirror element in the telescope assembly. These changes have already been ordered from the manufacturer. A fourth change is recommended to accomodate the combination of the other three and is described after laying the foundation for the change.

1. The New Grating

For ray components in the direction perpendicular to the ruling direction, the linearly ruled reflection grating used in MUSTANG obeys the formula

$$\sin(\theta) - \sin(i) = m\lambda L \qquad (56)$$

where L is the number of lines on the grating per unit length, λ is the wavelength of the incident light, m is the order of the reflection, i is the angle between the incident ray and the surface normal, and θ is the angle between the departing ray and the surface normal. The component of a ray traveling parallel to the rulings is simply reflected with an departure angle equal to the incidence angle. This instrument uses only the first-order path, so m is equal to one.

ISAAC incorporates a 4800 line/mm reflection grating instead of a 1200 line/mm grating. For 1800 Å light and i=0, the MUSTANG grating departure angle θ is 12.5°. For the same wavelength in ISAAC the departure angle θ is 35.2°. A similar increase in departure angle occurs for the 3400 Å case. MUSTANG was designed so that the 1800 Å to 3400 Å band fit on the detector in its entirety. For ISAAC to cover this band of wavelengths the grating must be rotated to correctly position the wavelengths on the detector, and the increased angular spread of the wavelengths with the new grating mandates the use of multiple grating positions.

At first glance, one might try to split the 1800-3400 Å band onto the detector with four different positions of the grating, since quadrupling the lines would make a band roughly four times wider. But this does not work because the incidence angle of the grating is changed by its rotation, such that the band grows even wider at the larger angles. To attain the range of the original MUSTANG seven bands would be required. The higher the band, the more the grating must be turned and the smaller the range of wavelengths included in the band, so much so that the last two bands together would only be 350 Å wide. To retain simplicity while enhancing performance, five bands are chosen to cover the range from 1800 to 3055 angstroms, each band operating with a fixed rotational angle of the grating. Note that when the entrance slit is narrowed and the parabolic mirror is substituted later, the grating positions and the bands do not change, since the band placement is required as a result of the grating change. Table 3 lists the characteristics of these bands.

Table 3. MUSTANG CHARACTERISTICS WITH 4800 LINES/MM GRATING, SPHERICAL TELESCOPE MIRROR AND 14 MICRON SLIT.

Band	Grating Angle	Wavelength (Å)	Position (cm)	Resolution (Å)
1	186.65°	1800	1.13	2.2
		1950	0.01	2.2
		2100	-1.23	2.4
2	191.5°	2100	1.18	2.1
		2240	0.04	2.2
		2380	-1.21	2.3
3	196.1°	2380	1.14	1.9
		2505	0.05	2.1
		2630	-1.18	2.3
4	200.4°	2630	1.10	1.8
		2740	0.04	2.0
		2850	-1.16	2.2
5	204.6°	2850	1.14	1.7
		2952	0.05	1.9
		3055	-1.22	2.2

Although a price must be paid for the added complexity, the new grating clearly reduces the instrument resolution by at least a factor of four over the nominal MUSTANG resolution of 10 Å, and in places by a factor of five. These data illustrate two trends. The first trend is that within each band the resolution worsens as the wavelength is increased. To show this effect, Equation 56 is differentiated with respect to θ to yield

$$d\lambda = \frac{1}{mL}\cos(\theta)d\theta \qquad (57)$$

Note that resolution is determined by the separation required to resolve adjacent wavelengths. As the wavelength increases, Equation 56 shows that the angle θ must also increase. If θ rises, then Equation 57 shows that the change of wavelength with θ is lowered, so the separation between adjacent wavelengths is reduced. Resolution is worsened by an increase in wavelength for a fixed grating position.

The second trend is for the resolution to improve from low bands to high bands. This is a direct result of the increased angular spread that results from using higher wavelength and higher

incidence angles. Because a smaller range of wavelengths fit on the detector in a higher band than fit in a lower band, the separation between wavelengths is inherently larger, and the resolution is smaller.

2. The Narrower Slit

The slit width constrains the field-of-view and the resultant line width at the detector by cropping the rays that tend to enlarge the beam. By cutting the slit in half, many more rays are cropped and the line width narrows. The price paid for this enhancement is intensity. If more light is prevented from reaching the detector, then the detector output signal is reduced and the instrument will be less effective in low light situations. If the 1800 Å line in Band 1 is analyzed with a slit 0.007 cm wide instead of the earlier 0.014 cm, the resolution improves from 2.17 angstroms to 1.594 angstroms. This 27% improvement is offset by a 51% loss of intensity, but because resolution is more critical than intensity, the narrower slit is a good choice. It is assumed that the other bands and wavelengths would change in a similar, if not identical fashion.

3. The Parabolic Telescope Mirror

Because the narrower slit cuts out such a large percentage of the available light, other avenues to raise the amount of light passing the slit were explored. Replacing the spherical telescope mirror with an off-axis parabolic mirror element focuses a great deal more light through the slit and subsequently raises the intensity of light at the detector. Table 4 shows the elements and their orientation in the MUSTANG after all of these changes have been incorporated. Resolution values and field-of-view measurements are presented in the detailed analysis below.

The plane mask in front of the parabolic element is used to create an off-axis parabolic element. Element areas must be centered about their local origins, so the parabolic element must be rather large to cover the area of the telescope mirror. By putting a square planar element in front of the active area of the parabolic to screen out any rays that would hit other parts of the mirror an off-axis element is formed.

Table 4. ISAAC CHARACTERISTICS WITH 4800 LINES/MM GRATING, PARABOLIC TELESCOPE MIRROR AND 7 MICRON SLIT

	Position of Center (cm)			Rotation Angles (deg.)			Mask Info (cm)	
Type	X	Y	Z	X	Y	Z	Width	Height
Plane Surface	0.000	0.000	21.194	0.000	0.000	0.000	2.500	2.500
Plane Mask	0.000	0.000	35.867	0.000	0.000	0.000	2.500	2.500
Parabolic Mirror	4.335	0.000	37.336	0.000	180.000	0.000	20.000	20.000
Plane Surface	4.335	0.000	24.471	0.000	-18.872	0.000	0.007	0.500
Spherical Mirror	11.288	0.000	13.713	0.000	-21.458	0.000	12.000	2.500
Plane Grating	6.795	0.000	23.479	0.000	186.65	0.000	2.500	2.500
Spherical Mirror	11.288	0.000	13.713	0.000	-21.458	0.000	12.000	2.500
Plane Surface	9.271	0.000	26.340	0.000	161.128	0.000	3.000	0.500

4. The Grating Adjustment

In the course of instrument analysis, it became clear that not all of the light that was passing the slit was reaching the detector. Since the slit should be the last restriction in the path of a ray, something after the slit was not working with all of the light. The reason for the loss of light was the grating itself. A 2.5 cm wide grating was more than sufficient for the original MUSTANG, since the slit and the series of spherical mirrors that preceded it in the optical path created a beam in all respects smaller than the grating. Because the parabolic mirror in ISAAC focuses a bigger input beam through the slit, the beam also expands to a larger width after passing it, so much so that the beam reaching the grating is larger than the grating itself. The requirement that the grating be tilted to accomodate varying wavelengths exacerbated the problem since the area of grating perpendicular to the beam cross-section was also reduced. The analysis shows that a larger grating is required to obtain the full benefit of the instrument optimization.

B. DETAILED ANALYSIS

For ISAAC, line placement describes the physical mapping of a wavelength to a particular position on the detector in a given band. Line placement and detector resolution go hand-in-hand for the new instrument so these analyses are presented first, followed by the analysis of resolution and field-of-view. Each band is covered in detail with the grating, entrance slit, and parabolic mirror changes incorporated. The field-of-view for the instrument should be the same regardless of wavelength or band, since the parabolic mirror and the slit determine the field-of-view, but because of the 2.5 cm grating size the resolution and the field-of-view are affected. The analysis shows the figures for the 2.5 cm grating case and shows the benefits of changing the ISAAC grating to one 3.5 cm wide.

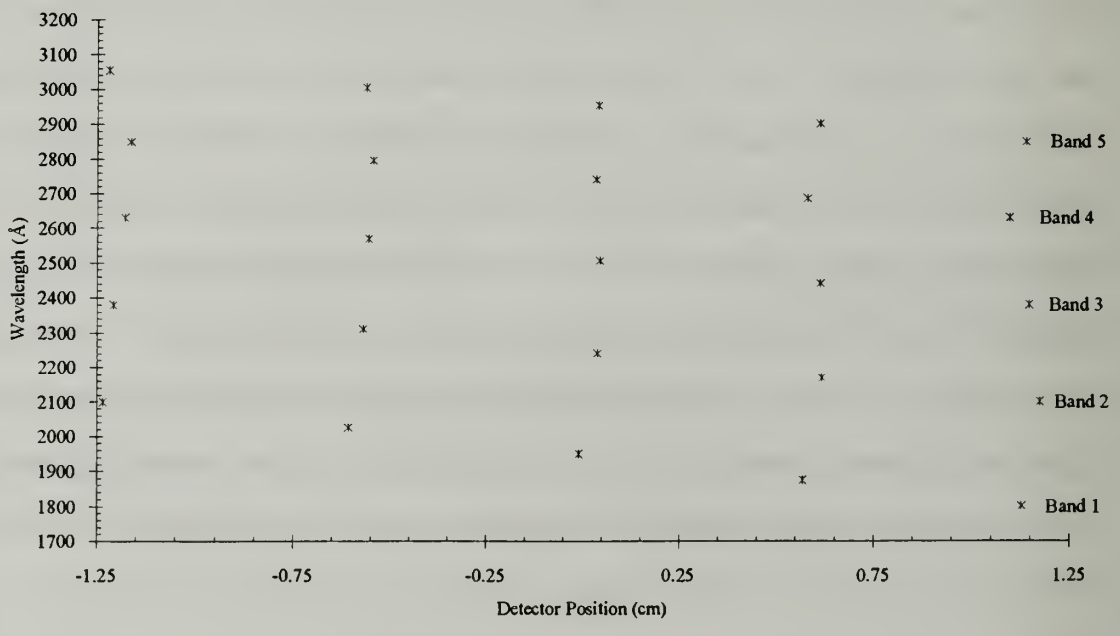


Figure 11. Line Placement in ISAAC Bands. Five points from each band show the wavelength response listed in Table 3.

1. Line Placement

The positioning of the lines in the bands shown in Table 3 remains unaltered by changing the grating size from 2.5 to 3.5 cm long, since the parabolic mirror and entrance slit changes do not affect the incidence angle of rays on the grating in any significant way. The band widths and angles were defined to allow the grating mirror to be stepped in discrete increments using, for instance, a cam assembly on a stepping motor. This way the line position on the detector can be more easily calibrated since the position is not a function of time, but of stepping motor angle. The bands are also designed so that the limiting wavelengths are not at the edges of the detector active region. This creates band overlap so that the lines of adjacent regions can be compared and so that the bands can be changed by small amounts to account for pixel failure or other reasons. Figure 11 shows the line placement in each band.

2. Resolution Measurements

To determine the resolution, the same procedure used earlier for the original MUSTANG was conducted, first for the 2.5 cm grating and then for the 3.5 cm grating. The FWHM plots for the band endpoints were used to determine the precise line position of the band limits. From this a dispersion factor was calculated. The FWHM's for three other lines in each band were computed to determine the linewidths, and the resolution was found as the product of the linewidth and the dispersion factor. Listed in Table 5 are the average resolutions for each of the five bands, with both the small and the large gratings.

The larger grating makes a significant difference in the resolution of the instrument because a lot of the light does not reach the detector with the small grating. Less light at the detector causes the peak to be smaller, and concomitantly forces the FWHM to be broader since the total width of the line remains relatively unchanged. With a grating capable of reflecting all of the light that passes the slit, overall performance is significantly improved.

Table 5. IMPROVED MUSTANG RESOLUTION VALUES (ISAAC INSTRUMENT WITH A 4800 LINES/MM GRATING, A PARABOLIC TELESCOPE MIRROR, AND A 7 MICRON SLIT).

Band	Minimum Wavelength (Å)	Maximum Wavelength (Å)	Resolution with 2.5 cm Grating (Å)	Resolution with 3.5 cm Grating (Å)
1	1800	2100	1.368	1.285
2	2100	2380	1.241	1.185
3	2380	2630	1.144	1.100
4	2630	2850	1.116	1.069
5	2850	3055	1.083	1.057

3. Field-of-View

The field-of-view for ISAAC is significantly smaller than for MUSTANG, at least in the X direction. The new field-of-view along the X-axis is 0.5 milliradians compared to the earlier 1.2 milliradians. The change in the Y-axis field-of-view from 37 to 36 milliradians is a small one created by the enhanced focusing power of the parabolic mirror. The change along the X-axis is striking, since it is a coupling of effects from the parabolic mirror and the smaller entrance slit. While the field-of-view is the same for both the 2.5 cm and the 3.5 cm cases, the intensity or number of hits upon the detector is clearly different, so the field-of-view curves provide a good mechanism for demonstrating the effect of the grating size.

The field-of-view should be independent of the grating size, but the intensity of light hitting the detector can obviously be affected if the grating is too small. Figures 12 and 13 show the X-axis and Y-axis fields-of-view for the instrument with the 2.5 cm grating and a 2500 Å Band 3 source. Figures 14 and 15 show the fields-of-view for the 3000 Å Band 5 line. For the band 5 case, with the same number of rays passing the slit, the number of hits upon the detector at every angle is reduced by approximately 5%. This can be shown in the following way. When the grating is rotated to accomodate Band 5 its area perpendicular to the beam is reduced and if the beam is too large it will be truncated at the edges of the grating; this is certainly what occurs for the 2.5 cm grating, as evidenced by the difference in detector hits between the two cases.

A bigger grating solves this problem, and Figures 16 and 17 show the number of rays hitting the detector for the 3.5 cm grating. No matter what band is used, with a 3.5 cm grating the number of hits is independent of wavelength as it should be. When the grating is enlarged, all of the light passing through the slit reaches the detector. The intensity of the received light is significantly higher than the 2.5 cm grating case, as much as 18% higher for the band five case and 14% higher for the band three case.

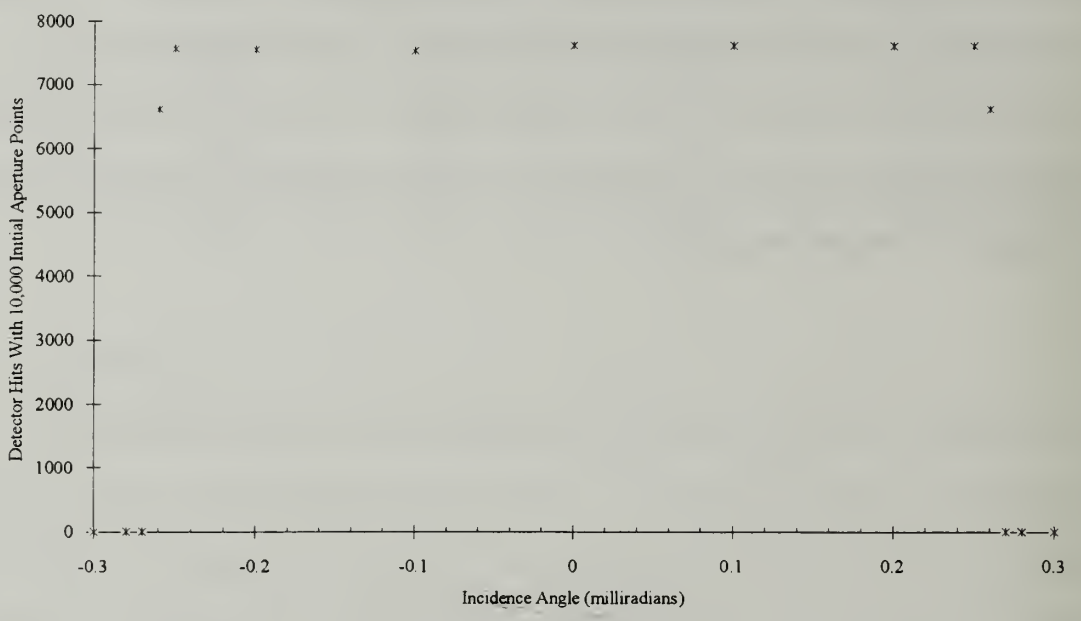


Figure 12. X-Axis Field-of-View for ISAAC Band 3, 2500 Å with the 2.5 cm Grating. The width of the envelope is 0.5 mrad.

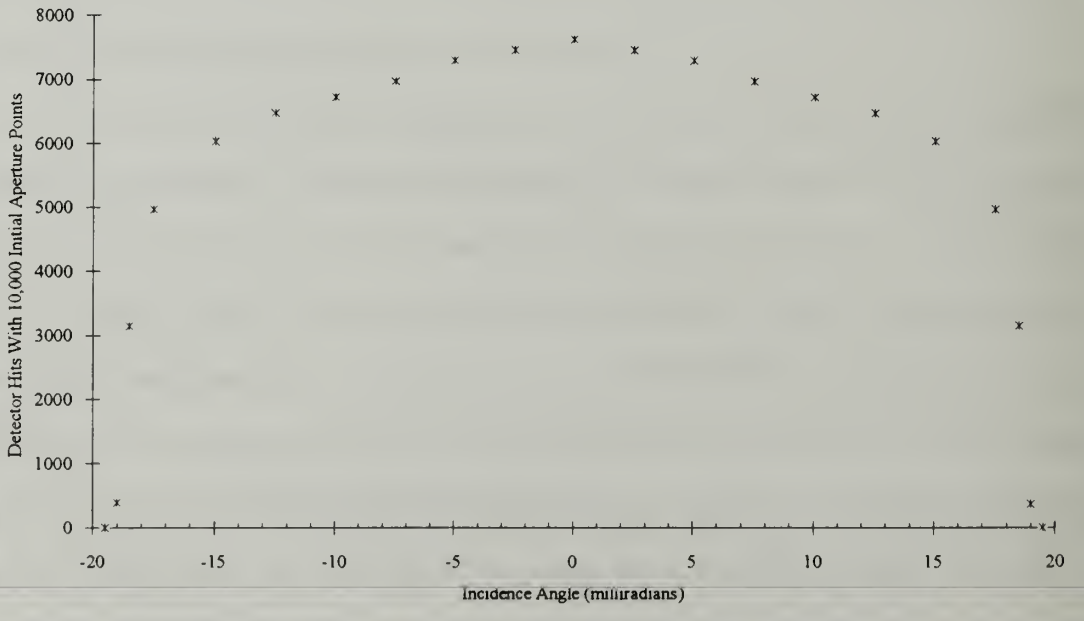


Figure 13. Y-Axis Field-of-View for ISAAC Band 3, 2500 Å with the 2.5 cm Grating. The width of the envelope is 36 mrad.

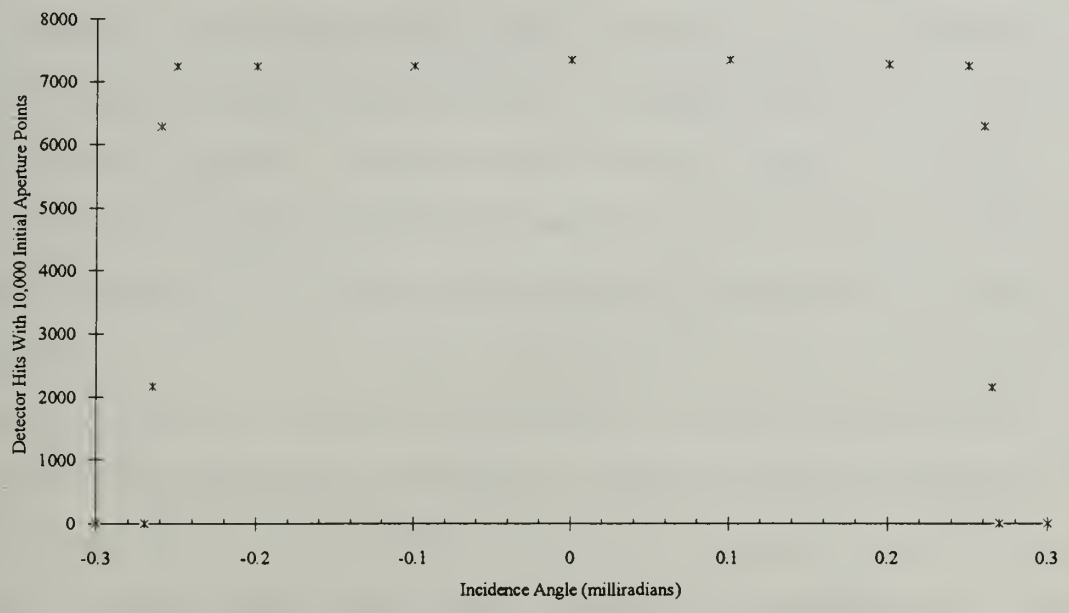


Figure 14. X-Axis Field-of-View for ISAAC Band 5, 3000 Å with the 2.5 cm Grating. The width of the envelope is 0.5 mrad.

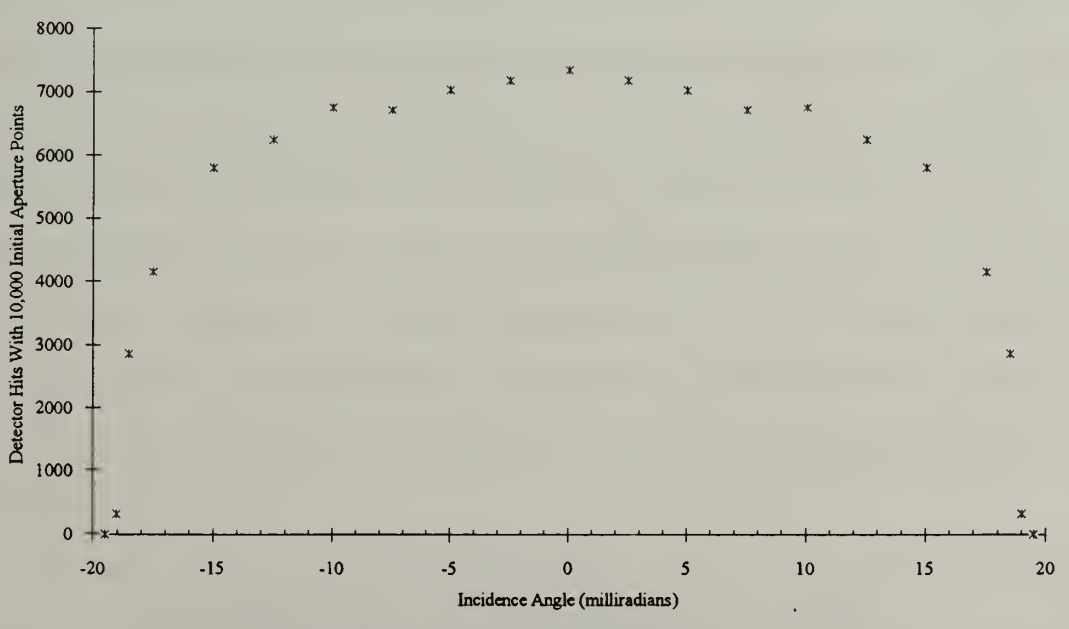


Figure 15. Y-Axis Field-of-View for ISAAC Band 5, 3000 Å with the 2.5 cm Grating. The width of the envelope is 36 mrad.

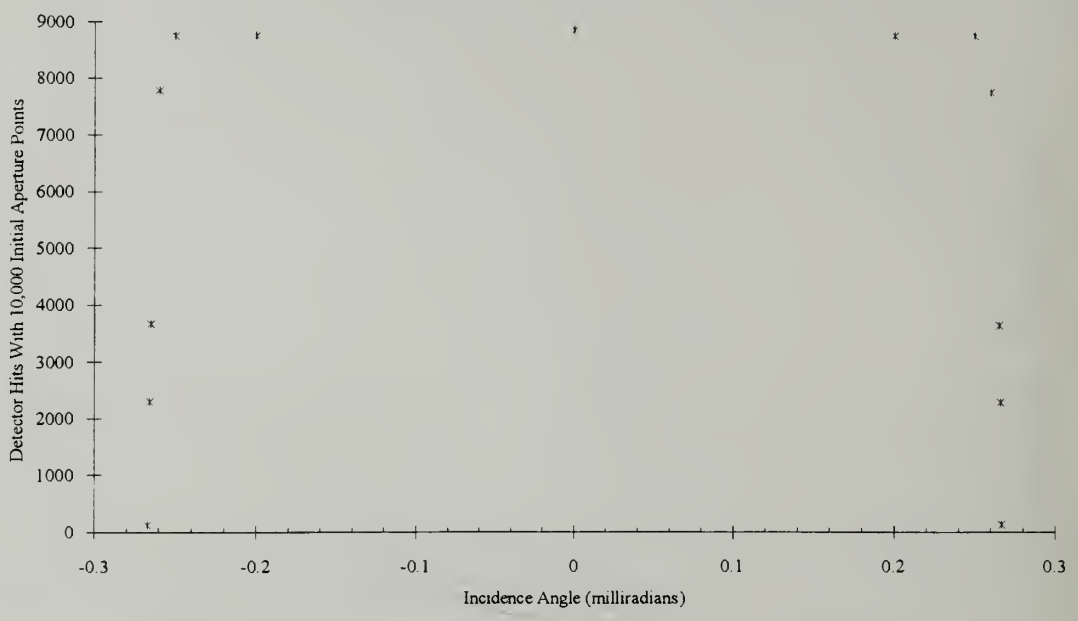


Figure 16. X-Axis Field-of-View for All ISAAC Bands with the 3.5 cm Grating. The width of the envelope is 0.5 mrad.

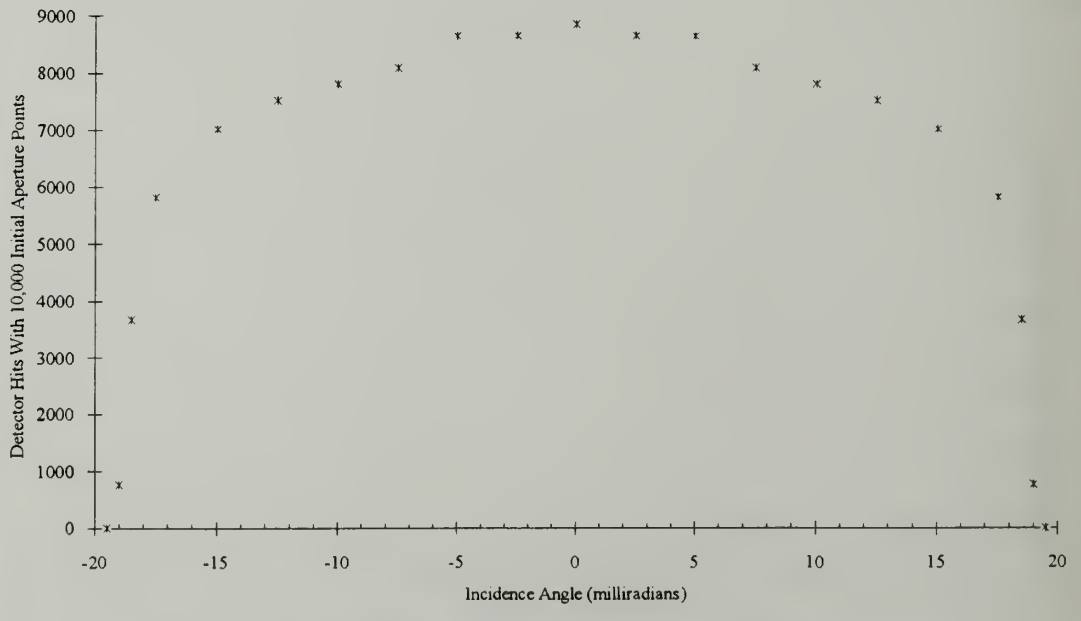


Figure 17. Y-Axis Field-of-View for All ISAAC Bands with the 3.5 cm Grating. The width of the envelope is 36 mrad.

VI. CONCLUSIONS AND RECOMMENDATIONS

DART is a versatile and user-friendly program that allows computer simulation of a wide variety of optical systems. The system input is very flexible as any number of rays or ray directions can be specified. The relative intensities of light at different wavelengths (i.e., the spectral irradiance) can be specified to simulate assorted wavelength profiles, like sodium lamps or ionospheric emissions. It can produce output for line profiles, intensity patterns, and interference determination. DART will draw the layout of the system under study and show on the layout the traces of the system rays. The output images, layouts and interference patterns can all be saved and used in other applications like word processors or spreadsheets. The program operates under the Windows platform on the IBM PC, so it is accessible to a large number of users who can easily learn to use DART since they will have already mastered the mechanics of the graphical interface.

DART accurately models the NPS MUSTANG instrument and provides new insight into parameters like the X-axis field-of-view that could not be accurately measured because of the extremely small values involved. Since DART has been shown to accurately model MUSTANG, it is a natural choice for analysis of the new ISAAC instrument. Design changes for ISAAC have been made that show that with minor alterations the MUSTANG instrument can be modified for satellite deployment and will achieve line resolutions 4 to 5 times better than MUSTANG. DART has shown that the use of a 2.5 cm square grating element in ISAAC will cause a partial loss of light at longer wavelengths, but that the loss is less than 15%. Since the detector response at assorted wavelengths is carefully calibrated prior to launch, this intensity loss can be accounted for through calibration. The extra expense required to modify the size of the grating is therefore not warranted.

DART is now being used to explore new interferometer designs. Work is underway at NPS to design another instrument that will measure the ionospheric emissions currently measured with

MUSTANG, but with a resolution improvement of 3 to 4 orders of magnitude (Cleary,1992). The interferometer design employs spatial heterodyne techniques to generate interference. It uses a grating to split the beam into two beams which are then reflected back to the grating to recombine. Interference occurs because the returning beams arrive at different angles normal to the grating surface, so that the phase difference between the returning beams at the grating varies with the distance across the surface. DART can correctly model the performance of these interferometers, since the system is an amplitude-splitting two beam system. DART is also useful in this work because complex wavelength distributions may be input to DART for solution; these solutions can be used to simulate actual system output so that analysis routines may be developed for the actual instrument.

Future research is needed to expand the capabilities of DART to include more surface types and to implement more analysis tools in the program. The modular design of the DART algorithms facilitates the creation of new surfaces and tools. Research is also needed for the development of the new interferometer, specifically for system modeling, prototype building, instrument electronic interface design, detector calibration and data analysis.

LIST OF REFERENCES

Anderson, C. K., *A Calibration of the Naval Postgraduate School Middle Ultraviolet Spectrograph and an Analysis of the OII 2470 Å Emission Obtained from Mid-Latitude Rocket Observations*, Master's Thesis, Naval Postgraduate School, Monterey, California, September 1990.

Chase, B., *Calibration of the Naval Postgraduate School MUSTANG Instrument*, Master's Thesis, Naval Postgraduate School, Monterey, California, September 1991.

Clayton, M. J., *Analysis of the Ultraviolet Emissions of Nitric Oxide from Mid-Latitude Rocket Observations*, Master's Thesis, Naval Postgraduate School, Monterey, California, June 1990.

Cleary, D., *The Middle Ultraviolet Spectrograph Experiment on the Argos Satellite*, NASA/DOD Space Flight Technical Interchange Meeting, Monterey, California, October 1992.

Hecht, E., *Optics*, Addison-Wesley: Reading, Massacheusetts, 1990.

Herzberger, M., J. Opt. Soc. Am. **41**, 805 (1951).

Jenkins, F.A. and White, H.F., *Fundamentals of Optics*, McGraw-Hill: New York, 1976.

Prinz, D.K., *Guidelines For Using The Raytracing Code of D. K. Prinz*, unpublished.

Spencer, G.H. and Murty, M.V.R.K., J. Opt. Soc. Am. **41**, 630 (1962).

INITIAL DISTRIBUTION LIST

1.	Defense Technical Information Center Cameron Station Alexandria, Virginia 22304-6145	2
2.	Library, Code 0142 Naval Postgraduate School Monterey, California 93943-5000	2
3.	Dr. D. D. Cleary Physics Department, PH-CL Naval Postgraduate School Monterey, California 93943-5000	3
4.	Dr. O. Biblarz Department of Aeronautics and Astronautics, AA-BI Naval Postgraduate School Monterey, California 93943-5000	1
5.	Lieutenant J. Dudley Atkinson IV 5415 Valley Forge Drive Baton Rouge, Louisiana 70808	2
6.	Dr. L. Paxton Johns Hopkins University Applied Physics Laboratory Johns Hopkins Road Laurel, Maryland 20723-6099	1

144-403


DEMCO

3 2768 00035902 0